

Cryogenic electro-optic interconnect for superconducting devices

Tobias Kippenberg (✉ tobias.kippenberg@epfl.ch)

École Polytechnique Fédérale de Lausanne <https://orcid.org/0000-0002-3408-886X>

Amir Youssefi

Swiss Federal Institute of Technology Lausanne, EPFL

Itay Shomroni

Ecole Polytechnique Federale de Lausanne (EPFL)

Yash Joshi

Ecole Polytechnique Federale de Lausanne (EPFL)

Nathan Bernier

Ecole Polytechnique Federale de Lausanne (EPFL)

Anton Lukashchuk

École Polytechnique Fédérale de Lausanne

Philipp Uhrich

Università di Trento <https://orcid.org/0000-0003-0747-368X>

Liu Qiu

École Polytechnique Fédérale de Lausanne <https://orcid.org/0000-0003-4345-4267>

Article

Keywords: optical fibers, cryogenic electro-optic, superconducting devices

Posted Date: August 17th, 2020

DOI: <https://doi.org/10.21203/rs.3.rs-55759/v1>

License:  This work is licensed under a Creative Commons Attribution 4.0 International License.

[Read Full License](#)

Version of Record: A version of this preprint was published at Nature Electronics on May 10th, 2021. See the published version at <https://doi.org/10.1038/s41928-021-00570-4>.

Cryogenic electro-optic interconnect for superconducting devices

Amir Youssefi^{1*}, Itay Shomroni^{1*}, Yash J. Joshi^{1,2}, Nathan Bernier¹, Anton

Lukashchuk¹, Philipp Uhrich¹, Liu Qiu¹, and Tobias J. Kippenberg^{1†}

¹*Institute of Physics, École Polytechnique Fédérale de Lausanne (EPFL), CH-1015 Lausanne, Switzerland*

²*Indian Institute of Science Education and Research, Pune 411008, India*

** These authors contributed equally to the work*

† E-mail: tobias.kippenberg@epfl.ch

Encoding information onto optical fields using electro-optical modulation is the backbone of modern telecommunication networks, offering vast bandwidth and low-loss transport via optical fibers [1]. For these reasons, optical fibers are also replacing electrical cables for short range communications within data centers [2]. Compared to electrical coaxial cables, optical fibers also introduce two orders of magnitude smaller heat load from room to milli-Kelvin temperatures, making optical interconnects based on electro-optical modulation an attractive candidate for interfacing superconducting quantum circuits [3–5] and hybrid superconducting devices [6]. Yet, little is known about optical modulation at cryogenic temperatures. Here we demonstrate a proof-of-principle cryogenic electro-optical interconnect, showing that currently employed Ti-doped lithium niobate phase modulators [7] are compatible with operation down to 800 mK—below the typical operation temperature of conventional microwave amplifiers based on high electron mobility transistors (HEMTs) [8, 9]—and maintain their room temperature Pockels coefficient. We utilize cryogenic electro-optical modulation to perform spectroscopy of a superconducting circuit optomechanical system, measuring optomechanically induced transparency (OMIT) [10–13]. In addition, we encode thermomechanical sidebands from the microwave domain onto an optical signal processed at room temperature. Although the currently achieved noise figure is significantly higher than that of a typical HEMT, substantial noise reduction should be attainable by harnessing recent advances in integrated modulators [14–17], by increasing the modulator length, or by using materials with a higher electro-optic coefficient [18, 19], leading to noise levels on par with HEMTs. Our work highlights the potential of electro-optical modulators

29 **for massively parallel readout for emerging quantum computing [3–6] or cryogenic classical**
 30 **computing [20] platforms.**

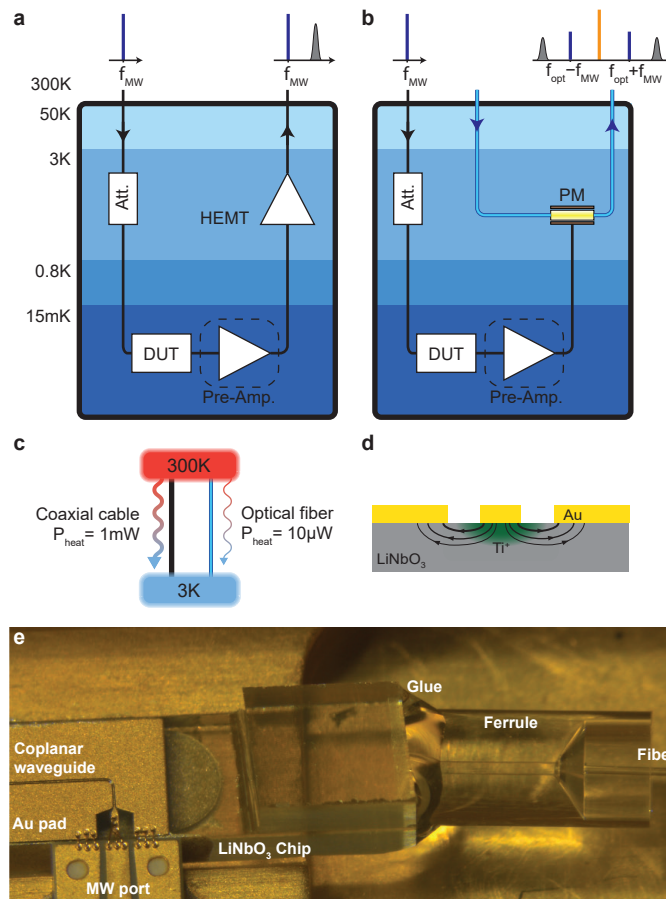


FIG. 1. Principle of a cryogenic electro-optical interconnect for readout of superconducting devices. **a**, Simplified schematic of a conventional readout of a device under test (DUT) in a dilution fridge using a cryogenic HEMT amplifier. The dashed box indicates an optional quantum-limited pre-amplifier not used in this work. The devices are interrogated by input microwave signals that are attenuated to reduce thermal noise, and amplified using an HEMT amplifier at 3 K. **b**, Principle of a cryogenic electro-optic readout scheme using an electro-optical phase modulator. The DUT is interrogated using the same microwave input line, but the microwave signals are converted to the optical domain at 3 K, reducing thermal load. **c**, Conducted heat through a typical cryogenic coaxial cable and optical fiber, between room temperature and 3 K. **d**, Schematic cross-section of a z-cut LiNbO₃ electro-optic phase modulator. **e**, Microscope photo of the commercial phase modulator used in the experiment, showing the coupling region between fiber and LiNbO₃ chip.

31 Optical modulators are ubiquitous in our information society and encode electrical signals in
 32 optical carriers that can be transported over fiber. Initially only used for long-haul communi-
 33 cations, optical fiber links are now also replacing electrical cables for short range communi-
 34 cations within data centers [21–23]. This is motivated by the high power consumption of electri-
 35 cal interconnects that spurred the development of optical interconnects based on silicon photon-

36 ics [22]. Such interconnects may also be used in the future for on-board chip-to-chip communica-
 37 tion [24, 25].

38 A similar challenge is foreseeable in superconducting quantum circuits, where recent ad-
 39 vances [3–5] have highlighted the potential associated with scaling superconducting qubit tech-
 40 nology [26]. Currently, significant efforts are underway to scale the number of qubits [27]. As
 41 a result, one of the challenges that future progress in superconducting circuits will face is to
 42 massively increase the number of microwave control and readout lines while preserving the base
 43 temperature and protecting qubits from thermal noise.

44 Figure 1a shows a prototypical measurement chain of a single superconducting device-under-
 45 test (DUT) that operates at the 15 mK stage of a dilution refrigerator. Coaxial cables are used to
 46 transmit output signals to the room temperature as well as to send control signals to the cold stages
 47 of the fridge. To read out GHz microwave signals, a high electron mobility transistor (HEMT) am-
 48 plifier with low-added-noise [$n_{\text{add}} \sim 10 \text{ quanta}/(\text{s} \cdot \text{Hz})$] is typically employed that operates at
 49 the 3 K stage and amplifies the DUT output signal for further processing outside the cryostat. Al-
 50 though HEMTs are not quantum-limited [8, 9], the development of Josephson junction-based pre-
 51 amplifiers [28–31] that operate at the 15 mK stage have allowed near-quantum-limited microwave
 52 amplification.

53 The presence of coaxial cables introduces additional heat load from room temperature into
 54 the cold stages of the refrigerator, which poses significant barrier to the scalability of such sys-
 55 tems [27]. In contrast, optical fibers have superior thermal insulation, reducing the heat load
 56 per line by two orders of magnitude (Fig. 1c). Optical fibers additionally exhibit ultralow signal
 57 losses, $\sim 0.2 \text{ dB/km}$, compared to $\sim 3 \text{ dB/m}$ at GHz frequencies for coaxial lines (compensated
 58 by the HEMT amplification). Note also that thermal noise is completely negligible at optical
 59 frequencies. Optical fibers could therefore provide a solution to scaling the number of lines with-
 60 out the concomitant heating. For this approach, a critical component are transducers that con-
 61 vert input microwave signals to the optical domain, which are compatible with low temperature
 62 operation and are sufficiently efficient to ensure low noise conversion of microwave to optical
 63 signals. Indeed, substantial efforts are underway to create quantum-coherent interfaces between
 64 the microwave and optical domains [32]. To date, quantum coherent conversion schemes based
 65 on piezo-electromechanical [33, 34], magneto-optical [35], and optomechanical [36–40] coupling

66 have been developed. In addition, schemes based on cavity electro-optics [41] have been demon-
 67 strated using bulk [42–44] or integrated [45–47] microwave cavities coupled via the Pockels effect
 68 to an optical cavity mode. Yet, all these schemes have in common that they transduce *narrowband*
 69 microwave signals to the optical domain. While this ability is critical for future quantum networks,
 70 an optical replacement for the currently employed HEMT amplifiers may be required for scaling
 71 control lines. One route is therefore to use *broadband* optical modulators as already used today
 72 in telecommunication networks. While this approach may yield lower conversion efficiency com-
 73 pared to systems employing narrowband resonant cavities, continued improvements in design, and
 74 new material systems, can render it competitive, especially given its relative simplicity.

75 Here we explore this potential and replace the HEMT amplifier with a LiNbO₃-based optical
 76 phase modulator (PM), the workhorse of modulator technology, in order to directly transduce the
 77 DUT microwave output signal onto sidebands around the optical carrier field (Fig. 1b), detectable
 78 using standard homodyne or heterodyne detection schemes at ambient temperatures. To illustrate
 79 the principle of the readout, we consider the operating principle of a PM. Optical PMs are based on
 80 the Pockels effect (Fig. 1d) and induce a phase shift on the input optical field $E_{\text{in}}(t)$, proportional
 81 to the voltage $V(t)$ applied on the input microwave port of the device,

$$E_{\text{out}}(t) = E_{\text{in}}(t)e^{-i\pi V(t)/V_{\pi}} \approx E_{\text{in}}(t)[1 - i\pi V(t)/V_{\pi}], \quad (1)$$

82 where the half-wave voltage V_{π} is the voltage at which the phase shift is π , and typical $V(t) \ll V_{\pi}$
 83 is assumed. The relation between microwave (field operator \hat{b}) and optical (field operator \hat{a}) photon
 84 flux spectral densities [48], $\bar{\mathcal{S}}_{bb}$ and $\bar{\mathcal{S}}_{aa}$ respectively, can be written as (see Appendix)

$$\bar{\mathcal{S}}_{aa}[\omega_{\text{opt}} \pm \omega_{\text{MW}}] = G \times (\bar{\mathcal{S}}_{bb}[\omega_{\text{MW}}] + n_{\text{add}}) \quad (2)$$

85 where ω_{MW} and ω_{opt} are the microwave signal and optical carrier frequencies, n_{add} is the added
 86 noise of the transducer (referred to the input), and the transduction gain G is the number of trans-
 87 duced optical photons per microwave input photon, given by (see Appendix):

$$G = P_{\text{opt}} \frac{\omega_{\text{MW}} \pi^2 Z_0}{\omega_{\text{opt}} 2V_{\pi}^2} \quad (3)$$

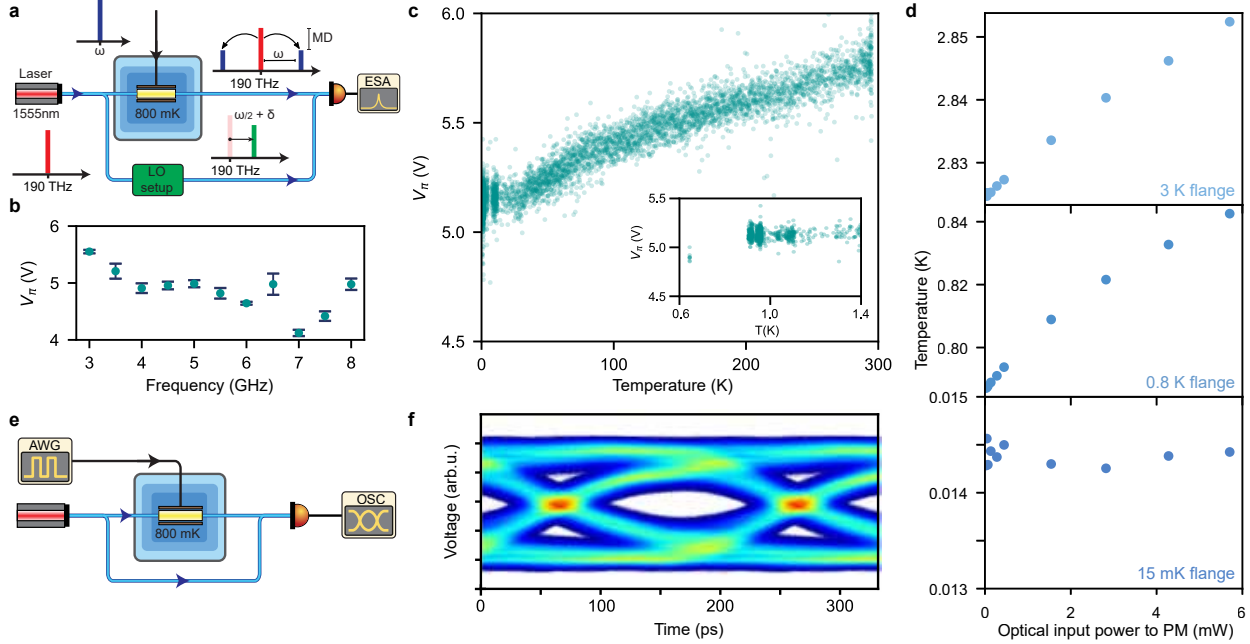


FIG. 2. Cryogenic characterization of a LiNbO₃ phase modulator. **a**, Experimental setup for low temperature characterization of the phase modulator. **b**, plot of V_{π} vs. frequency at 800 mK. **c**, Characterization of V_{π} at 5 GHz vs. temperature from room temperature to 800 mK. **d**, Measurement of heating due to optical dissipation when the phase modulator is mounted on the 800 mK flange. Plot of the steady state temperature vs. input laser power of the 3 K, 800 mK, and 15 mK flanges. **e**, Experimental setup for phase shift keying detection. RF signal from waveform generator is directly applied on a phase modulator. After homodyne detection the electrical signal is recorded on a fast oscilloscope. **f**, Eye-diagram of an optical signal phase-modulated at a rate of 5 GBaud, the bit error ratio is 5×10^{-5} .

88 where P_{opt} is the power of the optical carrier at the output of the PM, and Z_0 its input microwave
 89 impedance. In this experiment, we employ a commercial (Thorlabs LN65S-FC), z -cut travel-
 90 ing wave Ti-doped LiNbO₃ PM with specified bandwidth of 10 GHz and $V_{\pi} = 7.5$ V at 10 GHz
 91 (Fig. 1e). We use a 1555 nm fiber laser as the optical source. The typical incident optical power
 92 on the PM is 15 mW. The optical transmission of the PM was reduced during the first cooldown,
 93 and measured at 23%. Additional details on the cryogenic optical setup are given in the Appendix.

94 Previous works investigated the temperature dependence of the electro-optic coefficient and
 95 refractive index of congruent LiNbO₃ at low frequencies down to 7 K [49]. Commercial x -cut LN
 96 modulators were also tested down to 10 K, showing a slight change in V_{π} from its room tempera-
 97 ture value [50, 51]. Ref. [52] discusses the behavior of LiNbO₃ modulators with superconducting
 98 electrodes down to 4 K.

99 To date, however, such modulators have not been used in a dilution refrigerator to directly read
 100 out a superconducting device.

Characterization.

101

102 To characterize the electro-optic behavior of the device at cryogenic temperatures, we mount
 103 the PM on the 800 mK flange of the dilution fridge. We directly drive the microwave port of the PM
 104 at frequency ω_{MW} using a microwave source outside the fridge, generating sidebands around the
 105 optical carrier frequency (Fig. 2a). The half-wave voltage V_π is determined from the modulation
 106 depth MD, defined as the ratio of the power in one of sidebands to the power in the carrier,

$$V_\pi = \pi \sqrt{\frac{Z_0 P_{\text{MW}}}{2 \text{MD}}}, \quad (4)$$

107 where P_{MW} is the power at the microwave input port of the PM. We measure MD by beating the
 108 output optical signal with a local oscillator (LO) with frequency $\omega_{\text{opt}} + \omega_{\text{MW}}/2 + \delta$, generating two
 109 closely-spaced beatnotes at $\omega_{\text{MW}}/2 \pm \delta$, due to the carrier and the high-frequency sideband. Using
 110 Eq. (4) we extract V_π by sweeping the microwave power and measuring MD. Figure 2c shows V_π
 111 at 5 GHz monitored as the fridge is cooled down from room temperature to 800 mK, and Fig. 2b
 112 shows V_π at different frequencies at 800 mK. Importantly, V_π does not change substantially from
 113 the room temperature value.

114 To investigate the effect of heating caused by optical dissipation in the PM, we measured the
 115 steady state temperature of different flanges of the dilution fridge when the PM is mounted on the
 116 800 mK flange. The results are shown in Fig. 2d. In the Appendix, by comparing to a calibrated
 117 heater, we show that these temperature increases can be attributed to optical power loss within
 118 the PM package (and not, e.g. light leakage into the fridge volume). This allows quantitative
 119 comparison with, e.g., heat dissipation due to a HEMT, and suggests reduced heat load in high
 120 optical transmission devices.

121 To further assess the performance of the PM at 800 mK, we also performed a basic telecommu-
 122 nication experiment shown in Fig. 2e. An arbitrary waveform generator (AWG) directly drives the
 123 PM with a pseudo-random bit sequence at a rate of 5 GBaud. We beat the optical phase-modulated
 124 carrier output with its reference arm, effectively forming a Mach-Zehnder interferometer whose
 125 average transmission is tuned to the quadrature point by adjusting the laser frequency, and detect
 126 the electrical signal on the oscilloscope. Figure 2f shows an eye diagram obtained from 8×10^5

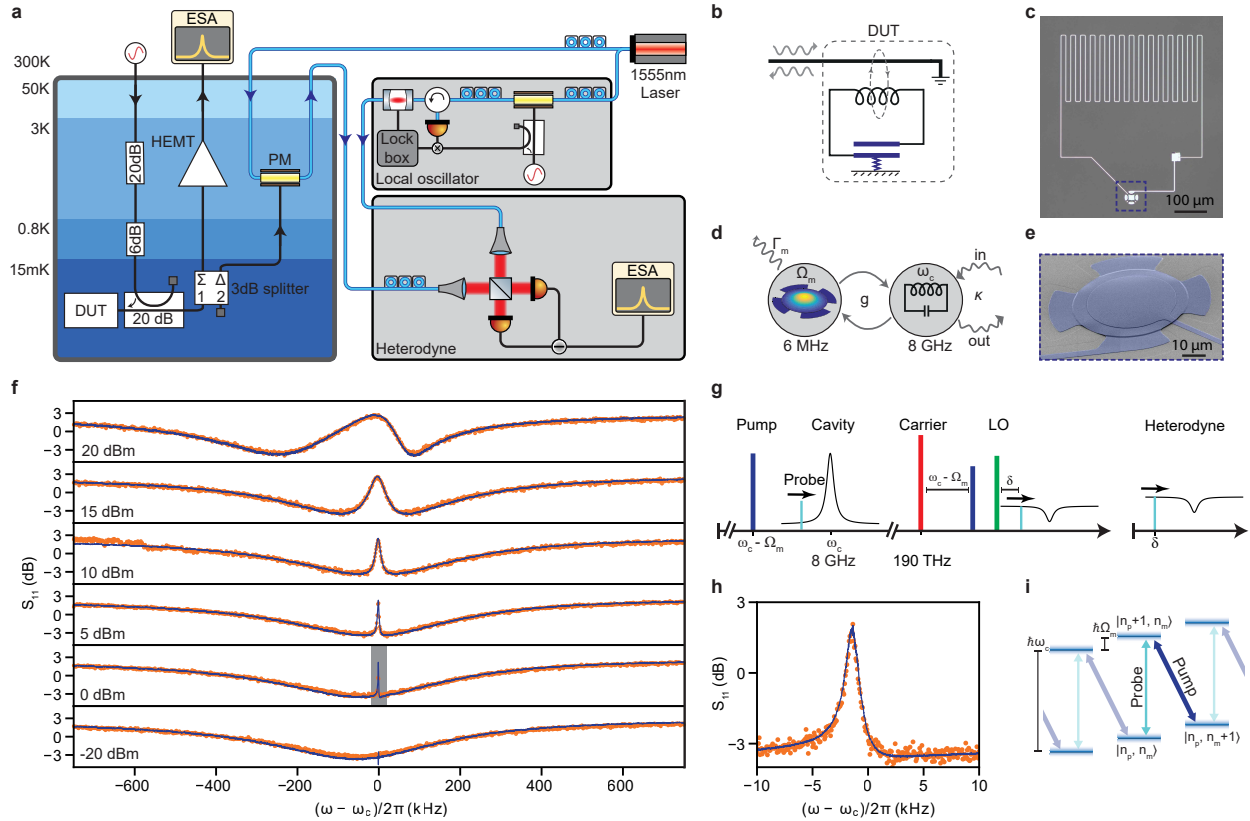


FIG. 3. Electro-optic readout of a coherent microwave spectrum of a superconducting electromechanical system. **a**, Experimental setup. Left: dilution fridge, right: optical setup. **b**, Electromechanical system used as a DUT. **c**, optical micrograph of the LC resonator. **d**, Modal diagram of the electromechanical system. **e**, scanning electron micrograph of the mechanically compliant capacitor. **f**, coherent measurement of the electromechanical resonance for increasing microwave pump powers of $(-20, 0, 5, 10, 15, 20)$ dBm at the source, from bottom to top respectively. The probe power is -20 dBm at the source. By increasing the pump power, the optomechanically induced transparency window emerges, and at stronger pump powers the modes get strongly coupled, leading to an avoided crossing effect. Blue lines correspond to HEMT readout and orange dots to optical readout. **g**, the frequency scheme for microwave tones, optical tones, and measured signal after heterodyning. **h**, high resolution measurement of the transparency window highlighted in **f** with the gray box. **i**, level scheme of the optomechanical system. The pump tone is tuned close to red sideband transitions, in which a mechanical excitation quantum is annihilated (mechanical occupation $n_m \rightarrow n_m - 1$) when a photon is added to the cavity (optical occupation $n_p \rightarrow n_p + 1$), therefore coupling the corresponding energy eigenstates. The probe tone probes reflection in which the mechanical oscillator occupation is unchanged. The pump tone modifies the response of the cavity and creates a transparency window appears on resonance (OMIT).

127 samples. The open eye diagram features no error bits, hence the upper bound on bit error ratio
 128 is limited by total amount of measured samples and can be estimated to be 5×10^{-5} with 95%
 129 confidence level [53]. These measurements clearly demonstrate that the cryogenic modulator still
 130 functions at 800 mK.

Optical Readout of Coherent Microwave Spectroscopy

131

132 Having established the cryogenic modulation properties, we next carry out a cryogenic inter-
 133 connect experiment, where the microwave output of a DUT is read out optically. As an example
 134 system we employ a superconducting electromechanical device in the form of a mechanically-
 135 compliant vacuum gap capacitor parametrically coupled to a superconducting microwave res-
 136 onator (Fig. 3a–e). These devices have been employed in a range of quantum electromechanical
 137 experiments, such as cooling the mechanical resonator to its quantum ground state [54], strong
 138 coupling between mechanical and microwave modes [13], squeezing of mechanical motion [55],
 139 and demonstration of the quantum entanglement in the mechanical motion [56, 57], as well as
 140 implementing mechanically mediated tunable microwave non-reciprocity [58] and quantum reser-
 141 voir engineering [59]. The microwave resonance (frequency $\omega_c \simeq 2\pi \times 8.2$ GHz and linewidth
 142 $\kappa \simeq 2\pi \times 3$ MHz) is coupled to the mechanical resonance (frequency $\Omega_m \simeq 2\pi \times 6$ MHz and
 143 linewidth $\Gamma_m \simeq 2\pi \times 10$ Hz) of the capacitor via electromechanical coupling [60] (Fig. 3d). The
 144 electromechanical coupling rate is $g = g_0\sqrt{\bar{n}_{\text{cav}}}$, where $g_0 \simeq 2\pi \times 150$ Hz is independently char-
 145 acterized [61] and \bar{n}_{cav} is intracavity microwave photon number, proportional to the microwave
 146 pump power. The system is inductively coupled to a microwave feed-line, enabling us to pump
 147 and read out the microwave mode in reflection.

148 To demonstrate the electro-optical readout technique, we perform two-tone spectroscopy and
 149 measure optomechanically induced transparency (OMIT) [10–12] (Fig. 3i) on the electromechan-
 150 ical sample, by applying a microwave pump tone on the lower motional sideband (red-detuned
 151 by Ω_m from the cavity resonance) and sweeping a second probe tone across the resonance. The
 152 strong pump damps the mechanical motion, resulting in a wider effective mechanical linewidth,
 153 $\Gamma_{\text{eff}} = \Gamma_m + 4g^2/\kappa$. The microwave pump modifies the cavity response due to the electromechani-
 154 cal coupling, resulting in a transparency window of width Γ_{eff} that appears on resonance, which we
 155 observe by the probe (Fig. 3g). We performed an OMIT experiment for different pump powers and
 156 observed the mechanical resonance via the transparency feature. In order to electro-optically read
 157 out the coherent response, the optical output is detected in a balanced heterodyne detector, using a
 158 frequency-shifted local oscillator (Fig. 3g). Note that this scheme allows resolving spectroscopic
 159 features finer than the laser linewidth (Fig. 3h). To compare the optical and HEMT readouts, the

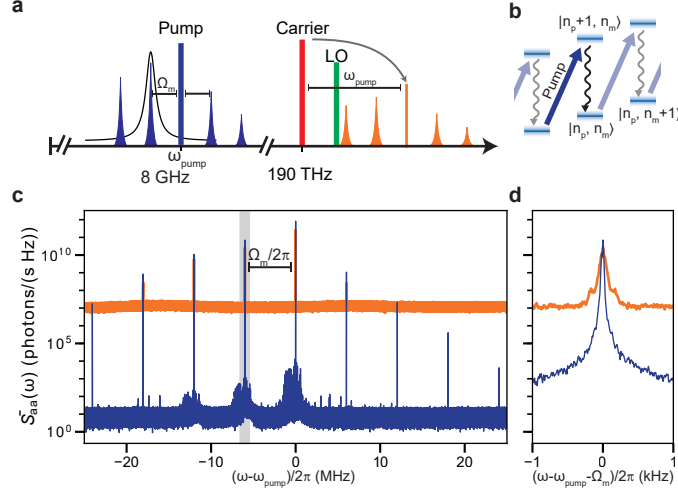


FIG. 4. Electro-optic readout of an incoherent microwave spectrum of a superconducting electromechanical system. **a**, Frequency-domain picture: a microwave tone pumps the electromechanical system on the upper motional sideband, inducing a parametric instability and generating mechanical sidebands equally spaced around the tone by the mechanical resonance frequency Ω_m . The phase modulator transfers the microwave spectrum on the optical signal, which is subsequently mixed with a local oscillator (LO) and detected via heterodyne detection. **b**, Level scheme showing electromechanically induced parametric instability. A blue-detuned pump photon scatters into an on-resonance photon and generates a phonon in the mechanical oscillator and causes anti-damping. At pump power above a certain threshold induces instability in the mechanical oscillator. **c**, Measured power spectral densities of the microwave pump (central peak) and mechanical sidebands detected by the HEMT (blue) and optical (orange) readouts. **d**, Enlargement of the gray-shaded area in **c**, showing the power spectral densities of the on-resonance mechanical sideband.

160 reflected signal is split and measured simultaneously using both techniques (Fig. 3a). Figure 3f
 161 shows the OMIT results, with excellent agreement between the optical and HEMT readouts. At
 162 high pump powers, when $g \sim \kappa$, we observe mode splitting as a result of strong coupling and
 163 mode-hybridization between the mechanical and microwave modes [13].

164

Optical Readout of an Incoherent Microwave Spectrum

165 Next, we employ our scheme to directly read out optically the power spectral density of a
 166 microwave signal emitted by the DUT. For this, we drive the mechanical oscillator into self-
 167 oscillation by pumping the system on its upper motional sideband, $\omega_{\text{pump}} = \omega_c + \Omega_m$, inducing
 168 a parametric instability [60, 62–64]. The output microwave spectrum features strong sidebands
 169 around the microwave pump, at integer multiples of the mechanical frequency (Fig. 4a,b). Fig-
 170 ure 4c shows these mechanical signals obtained simultaneously using both our optical readout and

171 the HEMT amplifier. We use the known properties of the HEMT to estimate the transduction gain
 172 G [Eq. (2)] of our optical readout. The blue trace in Fig. 4c shows the HEMT output referred back
 173 to its input using its known added noise, $n_{\text{add}}^{\text{HEMT}} \simeq 8 \text{ quanta}/(\text{s} \cdot \text{Hz})$, characterized independently.
 174 This calibration yields the HEMT input signal S , which is equal to the PM microwave input. The
 175 noise in the optically detected spectrum, referred to the optical output of the PM, is dominated by
 176 the optical shot noise, $1 \text{ quanta}/(\text{s} \cdot \text{Hz})$, for our $G \ll 1$. In this calibration, we can obtain G from
 177 the optical spectrum containing the transduced microwave signal GS . The orange trace in Fig. 4c
 178 shows the optical noise spectrum referred to the microwave input, and Fig. 4d shows a zoom-in
 179 of a single sideband. In this calibration, the signal areas in both measurements are equal to S .
 180 Further explanation of this calibration is given in the appendix. This yields $G = 0.9 \times 10^{-7}$, in
 181 good agreement with the theoretical value $G^{\text{theory}} = 3.5 \times 10^{-7}$ obtained from Eq. (3) using the
 182 measured output optical power, $P_{\text{opt}} = 1.1 \text{ mW}$ (optical efficiency of 5%, including losses in fiber
 183 connectors and heterodyne detection setup). We note that the frequency widening of the optically
 184 detected sidebands, observed in Fig. 4d, is due to fluctuations in the LO frequency, caused by
 185 the limited bandwidth of the locking setup in conjunction with using a minimal resolution band-
 186 width (RBW) of 1 Hz in the spectrum measurement. The integrated sideband power, however, is
 187 conserved. Improving the LO locking setup can reduce this effect.

188 The added noise in the transduction process is (see Appendix)

$$n_{\text{add}} = \frac{1}{2G} + n_{\text{th}}^{\text{MW}} + \frac{1}{2}, \quad (5)$$

189 where $n_{\text{th}}^{\text{MW}}$ is the average occupation of the thermal photonic bath due to the microwave fields.
 190 This gives $n_{\text{add}} \approx 6 \times 10^6$. The noise floor of the optical measurement in Fig. 4c is 60 dB above
 191 the HEMT readout. This is due to the very small gain $G \sim 10^{-7}$, caused by the large V_{π} and the
 192 limited optical power. However, there is much room for improvement in these parameters. Ref. 18
 193 reported a V_{π} -length product of 0.45 V cm in a BaTiO₃-based modulator, thus $V_{\pi} \sim 50 \text{ mV}$ can
 194 be realized in a $\sim 10 \text{ cm}$ device, possibly using low-loss superconducting electrodes [47, 52].
 195 The optical power can be increased arbitrarily in principle, however one needs to consider optical
 196 losses (mainly at the fiber-to-chip interfaces) that lead to heating. Considering a device with an
 197 improved optical transmission of 66% [65] and incident power of 15 mW, yields $P_{\text{opt}} \sim 10 \text{ mW}$.

198 This scenario achieves $G \sim 5 \times 10^{-2}$ [Eq. (3)], with $n_{\text{add}} \approx 20$ at 3 K, competitive with HEMT
 199 performance, while the heat load of 5 mW is half that of a typical cryogenic HEMT.

200 It is worth mentioning that many experiments utilize a near-quantum-limited pre-amplifier at
 201 the 15 mK stage (Fig. 1a,b). In this case, the noise added in the second amplification stage, referred
 202 to the input, is $\sim (G_{\text{PA}}G)^{-1}$ (see Appendix), where $G_{\text{PA}} \sim 10^3$ is the pre-amplifier gain [28–31].
 203 Thus, $G \gtrsim G_{\text{PA}}^{-1}$ suffices to preserve near-quantum-limited amplification (See Appendix).

204

Conclusions

205 We have demonstrated the viability of LiNbO₃ devices, currently-employed in the telecommu-
 206 nication market, as electro-optical interconnects in cryogenic platforms used in superconducting
 207 quantum technologies, in particular as viable alternative to HEMT amplifiers with the potential
 208 of reduced heat load. By interfacing a commercial PM to a circuit-electromechanical system that
 209 was previously used to perform quantum experiments, we implemented an electro-optical readout
 210 of this system. In addition, we quantified the gap between conventional microwave amplifiers and
 211 the electro-optical alternative. It is feasible that this gap be closed in the near future, by improved
 212 devices with lower V_π , resulting in a near-quantum-limited broadband microwave-to-optical inter-
 213 connect.

214

Appendix

215 **Quantum mechanical model for a phase modulator.** In the following, we derive a simple
 216 quantum description of the phase modulator to establish the quantum limits in transducing the
 217 input microwaves. The central assumption is that the linear regime stays valid, for sufficiently
 218 low input microwave powers. As such, the scattering equations linking inputs to output should be
 219 identical in both quantum and classical cases. We can use the known classical regime as a starting
 220 point, with the output optical field amplitude \hat{a}_{out} expressed as a function of the input optical field
 221 \hat{a}_{in} as

$$\hat{a}_{\text{out}} = e^{-i\pi V/V_\pi} \hat{a}_{\text{in}} \approx (1 - i\pi V/V_\pi) \hat{a}_{\text{in}}, \quad (\text{A.1})$$

222 where V is the classical voltage applied at the input and the half-wave voltage V_π is the voltage at
 223 which the phase modulator applies a phase shift of π . For the quantum model, the classical fields
 224 are replaced by their quantum equivalent. The microwave input becomes $\hat{V} = \sqrt{\hbar\omega_{\text{MW}}Z_0}(\hat{b} +$
 225 $\hat{b}^\dagger)/\sqrt{2}$ with \hat{b} the annihilation operator for the microwave field at frequency ω_{MW} traveling on a
 226 transmission line of impedance Z_0 . The optical input is $\hat{a}_{\text{in}} = \alpha e^{-i\omega_{\text{opt}}t} + \delta\hat{a}_{\text{in}}$, where α is the
 227 amplitude of the coherent carrier field of frequency ω_{opt} , with $|\alpha|^2 = P_{\text{opt}}/\hbar\omega_{\text{opt}}$, and $\delta\hat{a}_{\text{in}}$ carries
 228 the quantum fluctuations of the input optical field. Inserting the expressions in Eq. (A.1), we can
 229 compute $\delta\hat{a}_{\text{out}} = \hat{a}_{\text{out}} - \alpha e^{-i\omega_{\text{opt}}t}$, the quantum fluctuations of the output optical field, given by

$$\delta\hat{a}_{\text{out}} = \delta a_{\text{in}} - i\sqrt{G}e^{-i\omega_{\text{opt}}t}(\hat{b} + \hat{b}^\dagger) \quad (\text{A.2})$$

230 with the transduction gain G given by Eq. (3).

231 To understand the implications of Eq. (A.2) for the quantum noise in the transduction, we
 232 compute the power spectral density of the output optical field,

$$\mathcal{S}_{\delta a^\dagger \delta a}^{\text{out}}[\omega_{\text{opt}} + \omega_{\text{MW}}] = \mathcal{S}_{\delta a^\dagger \delta a}^{\text{in}}[\omega_{\text{opt}} + \omega_{\text{MW}}] + G(\mathcal{S}_{b^\dagger b}[\omega_{\text{MW}}] + \mathcal{S}_{bb^\dagger}[-\omega_{\text{MW}}]). \quad (\text{A.3})$$

233 The first term corresponds to the *added* quantum noise due to the input optical field. The second
 234 term contains contributions from the microwave frequency ω_{MW} , including both the signal and
 235 noise. The third term contains *added* microwave noise at frequency $-\omega_{\text{MW}}$, composed of thermal
 236 and quantum noise components, respectively $n_{\text{th}}^{\text{MW}} + 1/2$. Thus Eq. (A.3) can be simplified to

$$\mathcal{S}_{\delta a^\dagger \delta a}^{\text{out}}[\omega_{\text{opt}} + \omega_{\text{MW}}] = G \mathcal{S}_{b^\dagger b}[\omega_{\text{MW}}] + G \left(n_{\text{th}}^{\text{MW}} + \frac{1}{2} \right) + \frac{1}{2}. \quad (\text{A.4})$$

237 We emphasize two limiting cases. When $G \ll 1$, as in our experiment, the added noise is domi-
 238 nated by the input optical quantum noise, the last term in Eq. (A.4). In the opposite limit, $G \gg 1$,
 239 the added noise is dominated by the microwave input noise, and the signal-to-noise ratio is inde-
 240 pendent of G . In any case, the added noise referred to the input is given by Eq. (5).

241 **Calibration of the transduction gain.** Figure 5 illustrates the procedure of experimentally
 242 characterizing the transduction gain of our electro-optic transducer. The microwave signal is split
 243 equally into two parts S , fed to the HEMT amplifier and the PM respectively (Fig. 5a). The HEMT

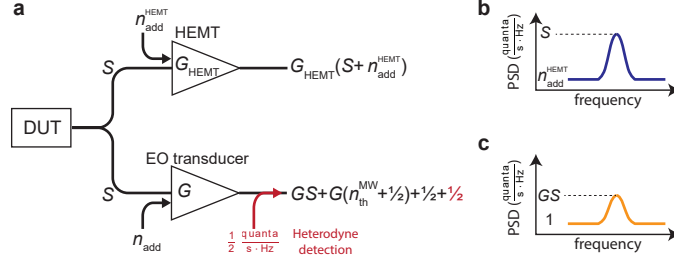


FIG. 5. **Illustration of the gain characterization procedure.** **a**, Propagation of the DUT signal through the system. **b**, Power spectral density of the HEMT output. **c**, Power spectral density of the optical heterodyne detector.

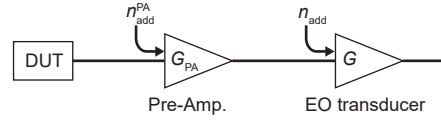


FIG. 6. Schematic signal flow when pre-amplifier is used.

244 added noise is characterized independently to be $n_{\text{add}}^{\text{HEMT}} = 8 \text{ quanta}/(\text{s} \cdot \text{Hz})$. We infer S from
 245 the spectrum of the HEMT amplified signal, referring the noise floor to $n_{\text{add}}^{\text{HEMT}}$ (Fig. 5b). In the
 246 PM branch, the added noise of the transduction is given by Eq. (5). The spectrum is detected using
 247 a balanced heterodyne detector, which adds $1/2 \text{ quanta}/(\text{s} \cdot \text{Hz})$ of noise (Fig. 5c). We can safely
 248 neglect $G(n_{\text{MW}} + 1/2)$ and consider the noise floor of the spectrum referred to the input of the
 249 heterodyne detector, i.e. $1 \text{ quanta}/(\text{s} \cdot \text{Hz})$. This allows us to calculate GS , and finally obtain G
 250 with knowledge of S from the HEMT measurement.

251 When using a quantum-limited pre-amplifiers before the electro-optical transducer (not done
 252 in our experiment), we can model the readout chain as shown in Fig. 6b. The total added noise of
 253 the readout chain is

$$n_{\text{add}}^{\text{total}} = n_{\text{add}}^{\text{PA}} + \frac{n_{\text{add}}}{G_{\text{PA}}} \simeq n_{\text{add}}^{\text{PA}} + \frac{1}{2G_{\text{PA}}G} \quad (\text{A.5})$$

254 Therefore when $G \simeq 1/G_{\text{PA}}$, the total added noise will be dominated by $n_{\text{add}}^{\text{PA}} \sim 1 \text{ quanta}/(\text{s} \cdot \text{Hz})$ [28–
 255 31] and the readout will be near-quantum-limited.

256 **Experimental details and heating measurements.** We use a fiber-coupled lithium niobate
 257 PM from Thorlabs, model LN65S, used as-is with no modifications. Note that the minimum spec-
 258 ified operating temperature is 0°C . The device sustained several cooldown-warmup cycles with
 259 reversible behavior in its optical transmission. We measured 25% reduction in the optical trans-
 260 mission at cryogenic relative to room temperature. The PM metallic box was tightly clamped to the

261 flange of the 800 mK or 3 K stage. We use a Bluefors LD-250 dilution refrigerator. The approxi-
 262 ate *available* cooling powers of the {15 mK, 800 mK, 3 K} stages are {12 μ W, 30 mW, 300 mW}.

263 Figure 2c shows the variation of V_π from room temperature to 800 mK, obtained during a
 264 cooldown of the dilution fridge and measured using the default thermometer on the 800 mK flange,
 265 located next to the heat exchanger, about 10 cm from the PM. In order to rule out possible tem-
 266 perature gradients, we mounted a calibrated thermometer next to the PM and monitored both
 267 thermometer readings during cooldown. Figure 7a shows the measured relative temperature dif-
 268 ference, which is less than $\sim 5\%$ throughout the cooldown. Note that this excludes pulse precool-
 269 ing and mixture condensation period when the temperature is unstable (shown for completeness
 270 in Fig. 7a).

271 Figure 2d shows the temperature increase of the 15 mK, 800 mK, and 3 mK stages of the dilu-
 272 tion fridge as a function of the optical power incident on the PM, which is mounted on the 800 mK
 273 stage. We performed a simple measurement to verify that this temperature increase can be ascribed
 274 to light absorbed in the PM body (and not, e.g, light leakage into the fridge volume), correspond-
 275 ing to the optical transmission (insertion loss) of the PM. We used the calibrated 120 Ω still heater
 276 built in the 800 mK stage to apply heat directly, we then repeated the measurement using optical
 277 input to the PM as the heating source (as in Fig. 2d). Figure 7a,b compares the results of this mea-
 278 surement, showing temperature increase in the 3 K and 800 mK stages (the latter recorded with the
 279 two separated thermometers) vs. dissipated power. In the case of optical heating, the dissipated
 280 power is computed directly from the incident power on the PM and its measured transmission of
 281 23%.

282 Figure 7b,c shows the result of this measurement. The optical heating shows a temperature
 283 increase of 13.3 mK/mW (6.5 mK/mW) at the 800 mK (3 K) stage (Fig.7a), while the resistive
 284 heating shows a temperature increase of 14.1 mK/mW (8.3 mK/mW) at the 800 mK (3 K) stage
 285 (Fig.7b). Thus heating due to operation of the electro-optical interconnect is very similar to local-
 286 ized, resistive heating.

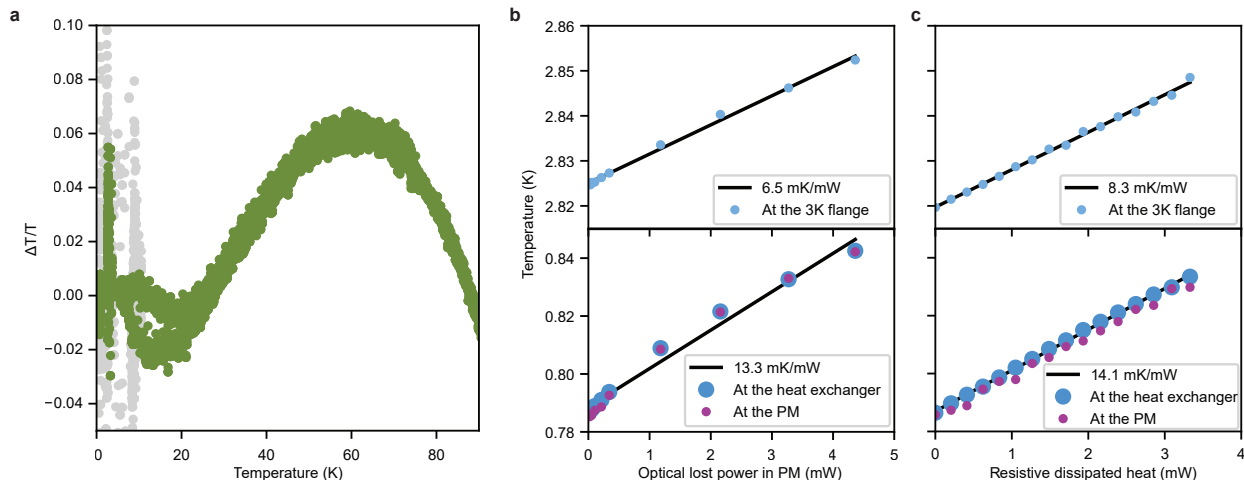


FIG. 7. **Heat dissipation and temperature gradients.** **a**, Relative temperature difference between PM box and heat exchanger, on 800 mK flange during a cooldown. The gray datapoints correspond to specific periods of pulse precooling and mixture condensation, where the temperature is unstable. **b**, Measurement of heating due to optical dissipation when the phase modulator is mounted on the 800 mK flange. **c**, Measurement of heating using a calibrated resistive heater mounted on the 800 mK flange.

287

Data availability statement

288

289

290

The code and data used to produce the plots within this paper will be available at a Zenodo open-access repository. All other data used in this study are available from the corresponding authors upon reasonable request.

291

ACKNOWLEDGMENTS

292

293

294

295

296

297

298

We thank Nils J. Engelsen for thorough reading of the manuscript. This work was supported by the European Union's Horizon 2020 research and innovation programme under grant agreement No. 732894 (FET Proactive HOT), and from the European Research Council (ERC) under the European Union's Horizon 2020 research and innovation programme (grant agreement No. 835329). This work was supported by funding from the Swiss National Science Foundation under grant agreement NCCR-QSIT: 51NF40_185902 and Sinergia grant no. 186364 (QuantEOM). The circuit electro-mechanical device was fabricated in the Center of MicroNanoTechnology (CMi) at

299 EPFL.

- 300 [1] Peter J Winzer, David T Neilson, and Andrew R Chraplyvy, “Fiber-optic transmission and network-
301 ing: the previous 20 and the next 20 years,” *Optics express* **26**, 24190–24239 (2018).
- 302 [2] Christoforos Kachris and Ioannis Tomkos, “A Survey on Optical Interconnects for Data Centers,”
303 *IEEE Communications Surveys Tutorials* **14**, 1021–1036 (2012).
- 304 [3] M. H. Devoret and R. J. Schoelkopf, “Superconducting Circuits for Quantum Information: An Out-
305 look,” *Science* **339**, 1169–1174 (2013).
- 306 [4] John M. Martinis, Michel H. Devoret, and John Clarke, “Quantum Josephson junction circuits and
307 the dawn of artificial atoms,” *Nature Physics* **16**, 234–237 (2020).
- 308 [5] Alexandre Blais, Steven M. Girvin, and William D. Oliver, “Quantum information processing and
309 quantum optics with circuit quantum electrodynamics,” *Nature Physics* **16**, 247–256 (2020).
- 310 [6] A. A. Clerk, K. W. Lehnert, P. Bertet, J. R. Petta, and Y. Nakamura, “Hybrid quantum systems with
311 circuit quantum electrodynamics,” *Nature Physics* **16**, 257–267 (2020).
- 312 [7] Ed L Wooten, Karl M Kissa, Alfredo Yi-Yan, Edmond J Murphy, Donald A Lafaw, *et al.*, “A review of
313 lithium niobate modulators for fiber-optic communications systems,” *IEEE Journal of selected topics*
314 *in Quantum Electronics* **6**, 69–82 (2000).
- 315 [8] Marian W Pospieszalski, Sander Weinreb, Roger D Norrod, and Ronald Harris, “Fets and hemts at
316 cryogenic temperatures-their properties and use in low-noise amplifiers,” *IEEE transactions on mi-*
317 *crowave theory and techniques* **36**, 552–560 (1988).
- 318 [9] KH George Duh, Marian W Pospieszalski, William F Kopp, Pin Ho, Amani A Jabra, *et al.*, “Ultra-
319 low-noise cryogenic high-electron-mobility transistors,” *IEEE transactions on electron devices* **35**,
320 249–256 (1988).
- 321 [10] S. Weis, R. Riviere, S. Deleglise, E. Gavartin, O. Arcizet, *et al.*, “Optomechanically induced trans-
322 parency,” *Science* **330**, 1520–1523 (2010).
- 323 [11] X. Zhou, F. Hocke, A. Schliesser, A. Marx, H. Huebl, *et al.*, “Slowing, advancing and switching of
324 microwave signals using circuit nanoelectromechanics,” *Nature Physics* **9**, 179–184 (2013).

- 325 [12] Amir H Safavi-Naeini, TP Mayer Alegre, Jasper Chan, Matt Eichenfield, Martin Winger, *et al.*, “Elec-
326 tromagnetically induced transparency and slow light with optomechanics,” *Nature* **472**, 69–73 (2011).
- 327 [13] J. D. Teufel, Dale Li, M. S. Allman, K. Cicak, A. J. Sirois, *et al.*, “Circuit cavity electromechanics in
328 the strong-coupling regime,” *Nature* **471**, 204–208 (2011).
- 329 [14] Cheng Wang, Mian Zhang, Xi Chen, Maxime Bertrand, Amirhassan Shams-Ansari, *et al.*, “Inte-
330 grated lithium niobate electro-optic modulators operating at cmos-compatible voltages,” *Nature* **562**,
331 101–104 (2018).
- 332 [15] Yang He, Qi-Fan Yang, Jingwei Ling, Rui Luo, Hanxiao Liang, Mingxiao Li, Boqiang Shen, Heming
333 Wang, Kerry Vahala, and Qiang Lin, “Self-starting bi-chromatic LiNbO₃ soliton microcomb,” *Optica*
334 **6**, 1138–1144 (2019).
- 335 [16] Frederik Thiele, Felix vom Bruch, Victor Quiring, Raimund Ricken, Harald Herrmann, Christof
336 Eigner, Christine Silberhorn, and Tim J. Bartley, “Cryogenic Electro-Optic Polarisation Conversion
337 in Titanium in-diffused Lithium Niobate Waveguides,” arXiv:2006.12078 [physics, physics:quant-ph]
338 (2020).
- 339 [17] Uttara Chakraborty, Jacques Carolan, Genevieve Clark, Darius Bunandar, Jelena Notaros, Michael R
340 Watts, and Dirk R Englund, “Cryogenic operation of silicon photonic modulators based on dc kerr
341 effect,” arXiv preprint arXiv:2007.03395 (2020).
- 342 [18] Stefan Abel, Felix Eltes, J. Elliott Ortmann, Andreas Messner, Pau Castera, *et al.*, “Large pockels
343 effect in micro- and nanostructured barium titanate integrated on silicon,” *Nature Materials* **18**, 42–47
344 (2019).
- 345 [19] Felix Eltes, Gerardo E. Villarreal-Garcia, Daniele Caimi, Heinz Siegwart, Antonio A. Gentile, *et al.*,
346 “An integrated cryogenic optical modulator,” arXiv:1904.10902 [physics] (2019), arXiv: 1904.10902.
- 347 [20] Alex I. Braginski, “Superconductor Electronics: Status and Outlook,” *Journal of Superconductivity*
348 and Novel Magnetism **32**, 23–44 (2019).
- 349 [21] Qixiang Cheng, Meisam Bahadori, Madeleine Glick, Sébastien Rumley, and Keren Bergman, “Recent
350 advances in optical technologies for data centers: a review,” *Optica* **5**, 1354–1370 (2018).
- 351 [22] David Thomson, Aaron Zilkie, John E Bowers, Tin Komljenovic, Graham T Reed, *et al.*, “Roadmap
352 on silicon photonics,” *Journal of Optics* **18**, 073003 (2016).

- 353 [23] Daniel J Blumenthal, Bengt-Erik Olsson, Giammarco Rossi, Timothy E Dimmick, Lavanya Rau, *et al.*,
354 “All-optical label swapping networks and technologies,” *Journal of Lightwave Technology* **18**, 2058
355 (2000).
- 356 [24] Chen Sun, Mark T Wade, Yunsup Lee, Jason S Orcutt, Luca Alloatti, *et al.*, “Single-chip micropro-
357 cessor that communicates directly using light,” *Nature* **528**, 534–538 (2015).
- 358 [25] David AB Miller, “Optical interconnects to silicon,” *IEEE Journal of Selected Topics in Quantum*
359 *Electronics* **6**, 1312–1317 (2000).
- 360 [26] Frank Arute, Kunal Arya, Ryan Babbush, Dave Bacon, Joseph C. Bardin, *et al.*, “Quantum supremacy
361 using a programmable superconducting processor,” *Nature* **574**, 505–510 (2019).
- 362 [27] Sebastian Krinner, Simon Storz, Philipp Kurpiers, Paul Magnard, Johannes Heinsoo, *et al.*, “Engineer-
363 ing cryogenic setups for 100-qubit scale superconducting circuit systems,” *EPJ Quantum Technology*
364 **6**, 1–29 (2019).
- 365 [28] Tsuyoshi Yamamoto, K Inomata, M Watanabe, K Matsuba, T Miyazaki, *et al.*, “Flux-driven josephson
366 parametric amplifier,” *Applied Physics Letters* **93**, 042510 (2008).
- 367 [29] Chris Macklin, K O’Brien, D Hover, ME Schwartz, V Bolkhovskiy, *et al.*, “A near-quantum-limited
368 josephson traveling-wave parametric amplifier,” *Science* **350**, 307–310 (2015).
- 369 [30] Irfan Siddiqi, R Vijay, F Pierre, CM Wilson, M Metcalfe, *et al.*, “Rf-driven josephson bifurcation
370 amplifier for quantum measurement,” *Physical review letters* **93**, 207002 (2004).
- 371 [31] MA Castellanos-Beltran, KD Irwin, GC Hilton, LR Vale, and KW Lehnert, “Amplification and
372 squeezing of quantum noise with a tunable josephson metamaterial,” *Nature Physics* **4**, 929–931
373 (2008).
- 374 [32] Nikolai Lauk, Neil Sinclair, Shabir Barzanjeh, Jacob P Covey, Mark Saffman, *et al.*, “Perspectives on
375 quantum transduction,” *Quantum Science and Technology* **5**, 020501 (2020).
- 376 [33] Wentao Jiang, Rishi N Patel, Felix M Mayor, Timothy P McKenna, Patricio Arrangoiz-Arriola, *et al.*,
377 “Lithium niobate piezo-optomechanical crystals,” *Optica* **6**, 845–853 (2019).
- 378 [34] Wentao Jiang, Christopher J Sarabalis, Yanni D Dahmani, Rishi N Patel, Felix M Mayor, *et al.*, “Ef-
379 ficient bidirectional piezo-optomechanical transduction between microwave and optical frequency,”
380 arXiv preprint arXiv:1909.04627 (2019).

- 381 [35] John G Bartholomew, Jake Rochman, Tian Xie, Jonathan M Kindem, Andrei Ruskuc, *et al.*, “On-
382 chip coherent microwave-to-optical transduction mediated by ytterbium in yvo ₄,” arXiv preprint
383 arXiv:1912.03671 (2019).
- 384 [36] A. P. Higginbotham, P. S. Burns, M. D. Urmev, R. W. Peterson, N. S. Kampel, *et al.*, “Harnessing
385 electro-optic correlations in an efficient mechanical converter,” *Nature Physics* **14**, 1038–1042 (2018).
- 386 [37] Moritz Forsch, Robert Stockill, Andreas Wallucks, Igor Marinković, Claus Gärtner, *et al.*,
387 “Microwave-to-optics conversion using a mechanical oscillator in its quantum ground state,” *Nature*
388 *Physics* **16**, 69–74 (2020).
- 389 [38] G Arnold, M Wulf, S Barzanjeh, ES Redchenko, A Rueda, *et al.*, “Converting microwave and telecom
390 photons with a silicon photonic nanomechanical interface,” arXiv preprint arXiv:2002.11628 (2020).
- 391 [39] Reed W Andrews, Robert W Peterson, Tom P Purdy, Katarina Cicak, Raymond W Simmonds, *et al.*,
392 “Bidirectional and efficient conversion between microwave and optical light,” *Nature Physics* **10**, 321–
393 326 (2014).
- 394 [40] Yiwen Chu and Simon Gröblacher, “A perspective on hybrid quantum opto-and electromechanical
395 systems,” arXiv preprint arXiv:2007.03360 (2020).
- 396 [41] Mankei Tsang, “Cavity quantum electro-optics,” *Physical Review A* **81**, 063837 (2010).
- 397 [42] Alfredo Rueda, Florian Sedlmeir, Michele C Collodo, Ulrich Vogl, Birgit Stiller, *et al.*, “Efficient
398 microwave to optical photon conversion: an electro-optical realization,” *Optica* **3**, 597–604 (2016).
- 399 [43] Alfredo Rueda, Florian Sedlmeir, Madhuri Kumari, Gerd Leuchs, and Harald G. L. Schwefel, “Res-
400 onant electro-optic frequency comb,” *Nature* **568**, 378–381 (2019).
- 401 [44] William Hease, Alfredo Rueda, Rishabh Sahu, Matthias Wulf, Georg Arnold, Harald G. L. Schwe-
402 fel, and Johannes M. Fink, “Cavity quantum electro-optics: Microwave-telecom conversion in the
403 quantum ground state,” arXiv:2005.12763 [physics, physics:quant-ph] (2020).
- 404 [45] Linran Fan, Chang-Ling Zou, Risheng Cheng, Xiang Guo, Xu Han, *et al.*, “Superconducting cavity
405 electro-optics: A platform for coherent photon conversion between superconducting and photonic
406 circuits,” *Science Advances* **4** (2018), 10.1126/sciadv.aar4994.
- 407 [46] Timothy P. McKenna, Jeremy D. Witmer, Rishi N. Patel, Wentao Jiang, Raphaël Van Laer, Patri-
408 cio Arrangoiz-Arriola, E. Alex Wollack, Jason F. Herrmann, and Amir H. Safavi-Naeini, “Cryo-
409 genic microwave-to-optical conversion using a triply-resonant lithium niobate on sapphire transducer,”

- 410 arXiv:2005.00897 [physics, physics:quant-ph] (2020).
- 411 [47] Jeffrey Holzgrafe, Neil Sinclair, Di Zhu, Amirhassan Shams-Ansari, Marco Colangelo, Yaowen Hu,
412 Mian Zhang, Karl K. Berggren, and Marko Lončar, “Cavity electro-optics in thin-film lithium niobate for efficient microwave-to-optical transduction,” arXiv:2005.00939 [physics, physics:quant-ph]
413 (2020).
- 414
- 415 [48] A. A. Clerk, M. H. Devoret, S. M. Girvin, Florian Marquardt, and R. J. Schoelkopf, “Introduction to
416 quantum noise, measurement, and amplification,” *Reviews of Modern Physics* **82**, 1155–1208 (2010).
- 417 [49] Christian Herzog, Gorazd Poberaj, and Peter Günter, “Electro-optic behavior of lithium niobate at
418 cryogenic temperatures,” *Optics Communications* **281**, 793–796 (2008).
- 419 [50] Jeffrey D. Morse, Kent George McCammon, Charles F. McConaghy, Don A. Masquelier, Henry E.
420 Garrett, *et al.*, “Characterization of lithium niobate electro-optic modulators at cryogenic tempera-
421 tures,” in *Design, Simulation, and Fabrication of Optoelectronic Devices and Circuits*, Vol. 2150,
422 edited by Mario Nicola Armenise, International Society for Optics and Photonics (SPIE, 1994) pp.
423 283–291.
- 424 [51] C. McConaghy, M. Lowry, R.A. Becker, and B.E. Kincaid, “The performance of pigtailed annealed
425 proton exchange linbo 3 modulators at cryogenic temperatures,” *IEEE Photonics Technology Letters*
426 **8**, 1480–1482 (1996).
- 427 [52] K. Yoshida, Y. Kanda, and S. Kohjiro, “A traveling-wave-type LiNbO₃ optical modulator with su-
428 perconducting electrodes,” *IEEE Transactions on Microwave Theory and Techniques* **47**, 1201–1205
429 (1999).
- 430 [53] Keysight. How to measure BER (2018).
- 431 [54] J. D. Teufel, T. Donner, Dale Li, J. W. Harlow, M. S. Allman, *et al.*, “Sideband cooling of microme-
432 chanical motion to the quantum ground state,” *Nature* **475**, 359–363 (2011).
- 433 [55] E. E. Wollman, C. U. Lei, A. J. Weinstein, J. Suh, A. Kronwald, *et al.*, “Quantum squeezing of motion
434 in a mechanical resonator,” *Science* **349**, 952–955 (2015).
- 435 [56] CF Ockeloen-Korppi, E Damskäg, J-M Pirkkalainen, M Asjad, AA Clerk, *et al.*, “Stabilized entan-
436 glement of massive mechanical oscillators,” *Nature* **556**, 478–482 (2018).
- 437 [57] Shabir Barzanjeh, ES Redchenko, Matilda Peruzzo, Matthias Wulf, DP Lewis, *et al.*, “Stationary
438 entangled radiation from micromechanical motion,” *Nature* **570**, 480–483 (2019).

- 439 [58] N. R. Bernier, L. D. Tóth, A. Koottandavida, M. A. Ioannou, D. Malz, *et al.*, “Nonreciprocal reconfig-
440 urable microwave optomechanical circuit,” *Nature Communications* **8** (2017), 10.1038/s41467-017-
441 00447-1.
- 442 [59] L. D. Tóth, N. R. Bernier, A. Nunnenkamp, A. K. Feofanov, and T. J. Kippenberg, “A dissipative
443 quantum reservoir for microwave light using a mechanical oscillator,” *Nature Physics* **13**, 787–793
444 (2017).
- 445 [60] Markus Aspelmeyer, Tobias J Kippenberg, and Florian Marquardt, “Cavity optomechanics,” *Reviews*
446 *of Modern Physics* **86**, 1391 (2014).
- 447 [61] Nathan R Bernier, *Multimode microwave circuit optomechanics as a platform to study coupled quan-*
448 *tum harmonic oscillators*, doctoral dissertation, EPFL (2018), section 3.5.2.
- 449 [62] Florian Marquardt, JGE Harris, and Steven M Girvin, “Dynamical multistability induced by radia-
450 tion pressure in high-finesse micromechanical optical cavities,” *Physical Review Letters* **96**, 103901
451 (2006).
- 452 [63] Tal Carmon, Hossein Rokhsari, Lan Yang, Tobias J Kippenberg, and Kerry J Vahala, “Temporal
453 behavior of radiation-pressure-induced vibrations of an optical microcavity phonon mode,” *Physical*
454 *Review Letters* **94**, 223902 (2005).
- 455 [64] D Cattiaux, X Zhou, S Kumar, I Golokolenov, RR Gazizulin, *et al.*, “Beyond linear coupling in mi-
456 crowave optomechanics,” arXiv preprint arXiv:2003.03176 (2020).
- 457 [65] Commercial PMs with typical insertion loss < 2 dB, ($> 63\%$ transmission), at room temperature are
458 already available.

Figures

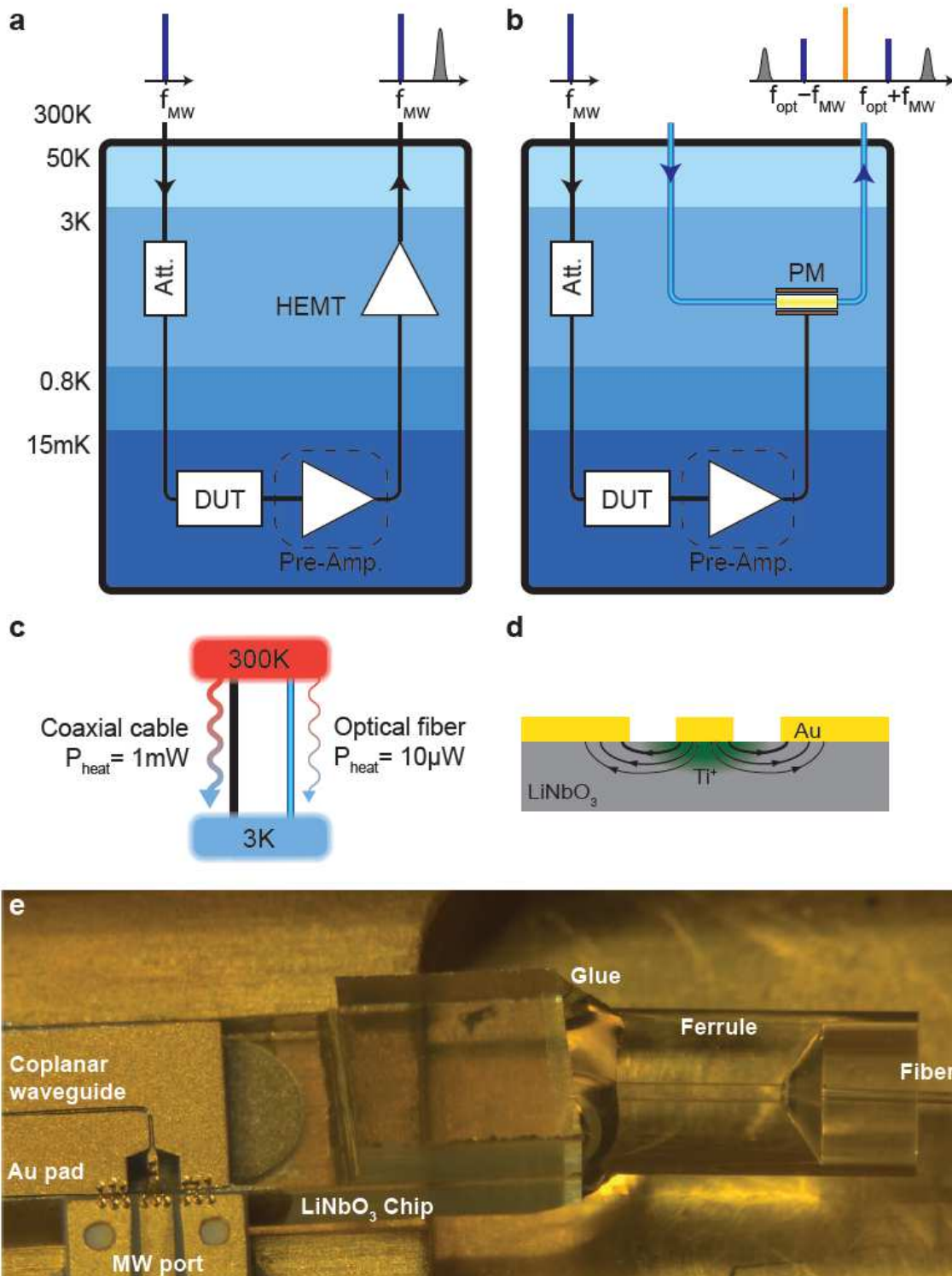


Figure 1

Principle of a cryogenic electro-optical interconnect for readout of superconducting devices. a, Simplified schematic of a conventional readout of a device under test (DUT) in a dilution fridge using a cryogenic HEMT amplifier. The dashed box indicates an optional quantum-limited pre-amplifier not used in this

work. The devices are interrogated by input microwave signals that are attenuated to reduce thermal noise, and amplified using an HEMT amplifier at 3K. b, Principle of a cryogenic electro-optic readout scheme using an electro-optical phase modulator. The DUT is interrogated using the same microwave input line, but the microwave signals are converted to the optical domain at 3 K, reducing thermal load. c, Conducted heat through a typical cryogenic coaxial cable and optical fiber, between room temperature and 3K. d, Schematic cross-section of a z-cut LiNbO₃ electro-optic phase modulator. e, Microscope photo of the commercial phase modulator used in the experiment, showing the coupling region between fiber and LiNbO₃ chip.

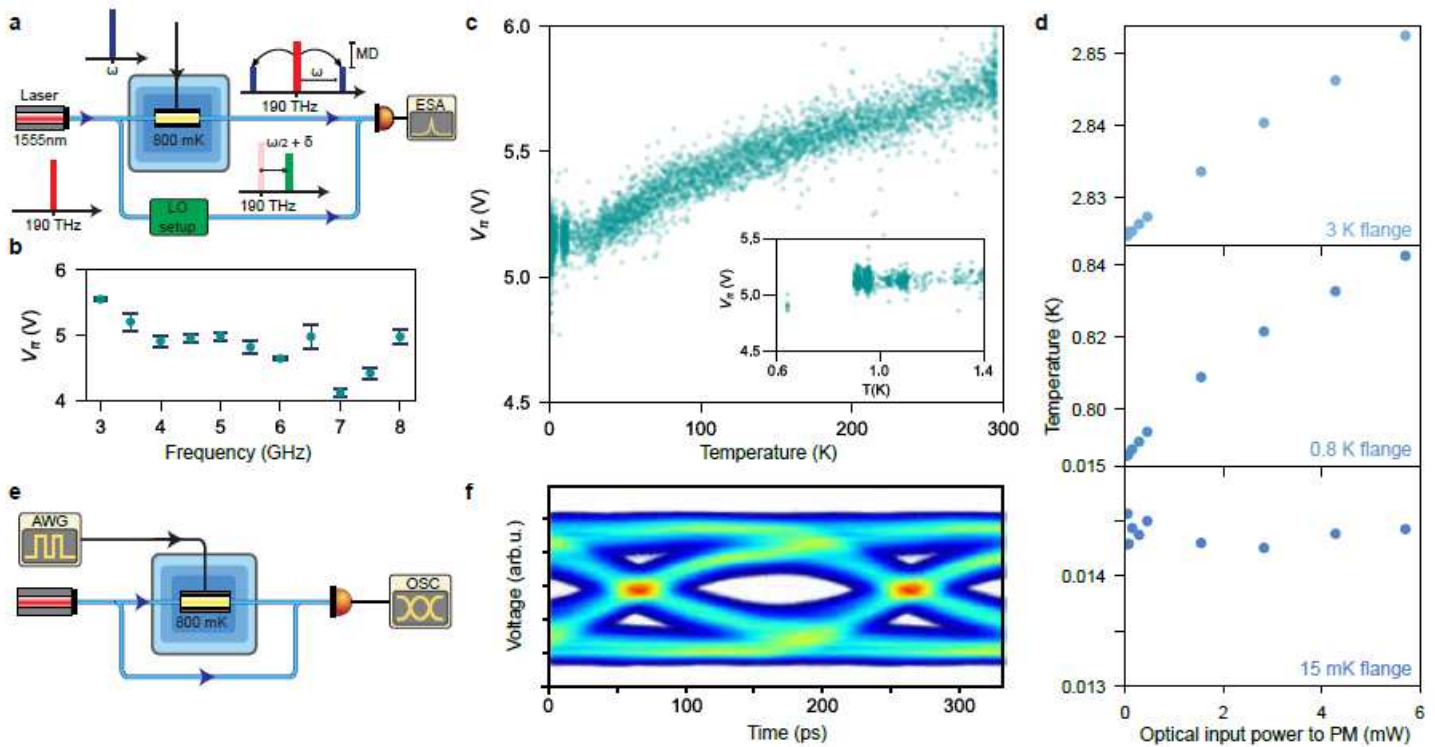


Figure 2

Cryogenic characterization of a LiNbO₃ phase modulator. a, Experimental setup for low temperature characterization of the phase modulator. b, plot of V_{π} vs. frequency at 800mK. c, Characterization of V_{π} at 5 GHz vs. temperature from room temperature to 800mK. d, Measurement of heating due to optical dissipation when the phase modulator is mounted on the 800mK flange. Plot of the steady state temperature vs. input laser power of the 3K, 800mK, and 15mK flanges. e, Experimental setup for phase shift keying detection. RF signal from waveform generator is directly applied on a phase modulator. After homodyne detection the electrical signal is recorded on a fast oscilloscope. f, Eye-diagram of an optical signal phase-modulated at a rate of 5 GBaud, the bit error ratio is 5×10^{-5} .

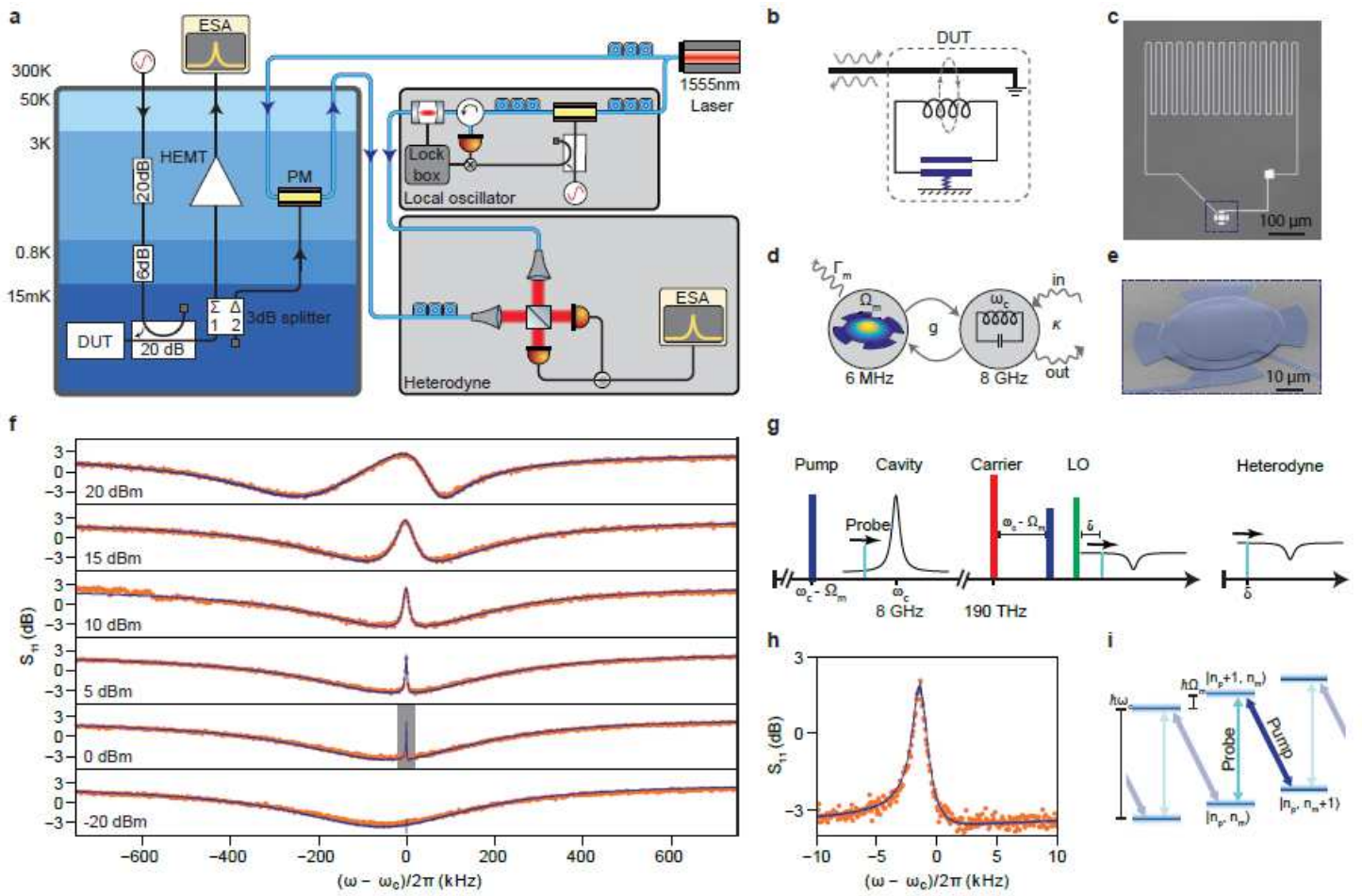


Figure 3

Electro-optic readout of a coherent microwave spectrum of a superconducting electromechanical system. a, Experimental setup. Left: dilution fridge, right: optical setup. b, Electromechanical system used as a DUT. c, optical micrograph of the LC resonator. d, Modal diagram of the electromechanical system. e, scanning electron micrograph of the mechanically compliant capacitor. f, coherent measurement of the electromechanical resonance for increasing microwave pump powers of (−20; 0; 5; 10; 15; 20)dBm at the source, from bottom to top respectively. The probe power is −20 dBm at the source. By increasing the pump power, the optomechanically induced transparency window emerges, and at stronger pump powers the modes get strongly coupled, leading to an avoided crossing effect. Blue lines correspond to HEMT readout and orange dots to optical readout. g, the frequency scheme for microwave tones, optical tones, and measured signal after heterodyning. h, high resolution measurement of the transparency window highlighted in f with the gray box. i, level scheme of the optomechanical system. The pump tone is tuned close to red sideband transitions, in which a mechanical excitation quantum is annihilated (mechanical occupation $n_m \rightarrow n_m - 1$) when a photon is added to the cavity (optical occupation $n_p \rightarrow n_p + 1$), therefore coupling the corresponding energy eigenstates. The probe tone probes reflection in which the mechanical oscillator occupation is unchanged. The pump tone modifies the response of the cavity and creates a transparency window appears on resonance (OMIT).

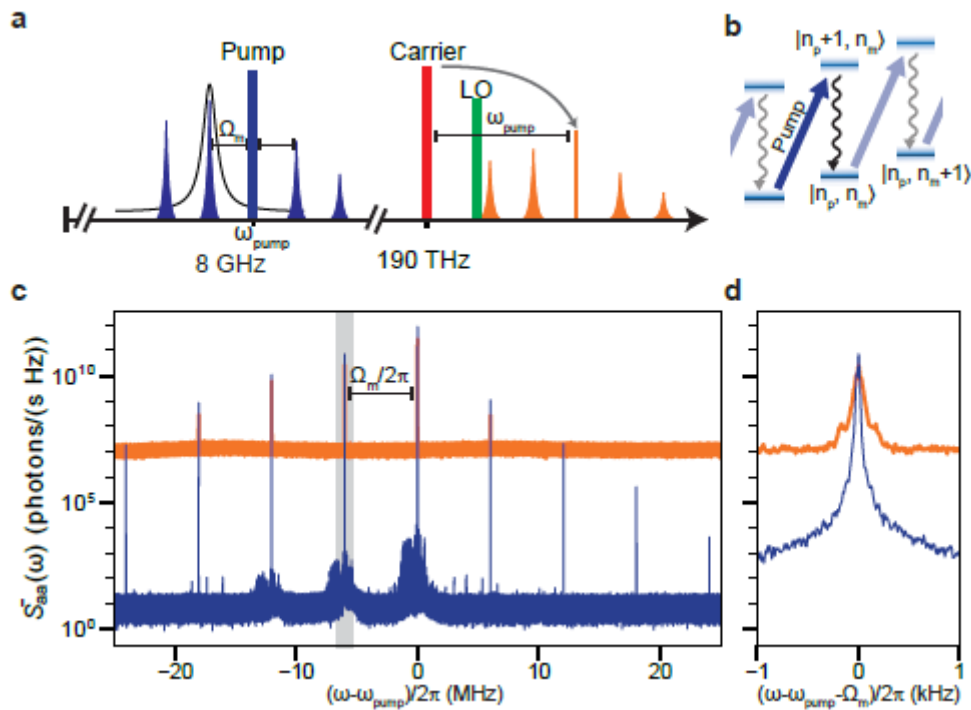


Figure 4

Electro-optic readout of an incoherent microwave spectrum of a superconducting electromechanical system. a, Frequency-domain picture: a microwave tone pumps the electromechanical system on the upper motional sideband, inducing a parametric instability and generating mechanical sidebands equally spaced around the tone by the mechanical resonance frequency Ω_m . The phase modulator transfers the microwave spectrum on the optical signal, which is subsequently mixed with a local oscillator (LO) and detected via heterodyne detection. b, Level scheme showing electromechanically induced parametric instability. A blue-detuned pump photon scatters into an on resonance photon and generates a phonon in the mechanical oscillator and causes anti-damping. At pump power above a certain threshold induces instability in the mechanical oscillator. c, Measured power spectral densities of the microwave pump (central peak) and mechanical sidebands detected by the HEMT (blue) and optical (orange) readouts. d, Enlargement of the gray-shaded area in c, showing the power spectral densities of the on-resonance mechanical sideband.

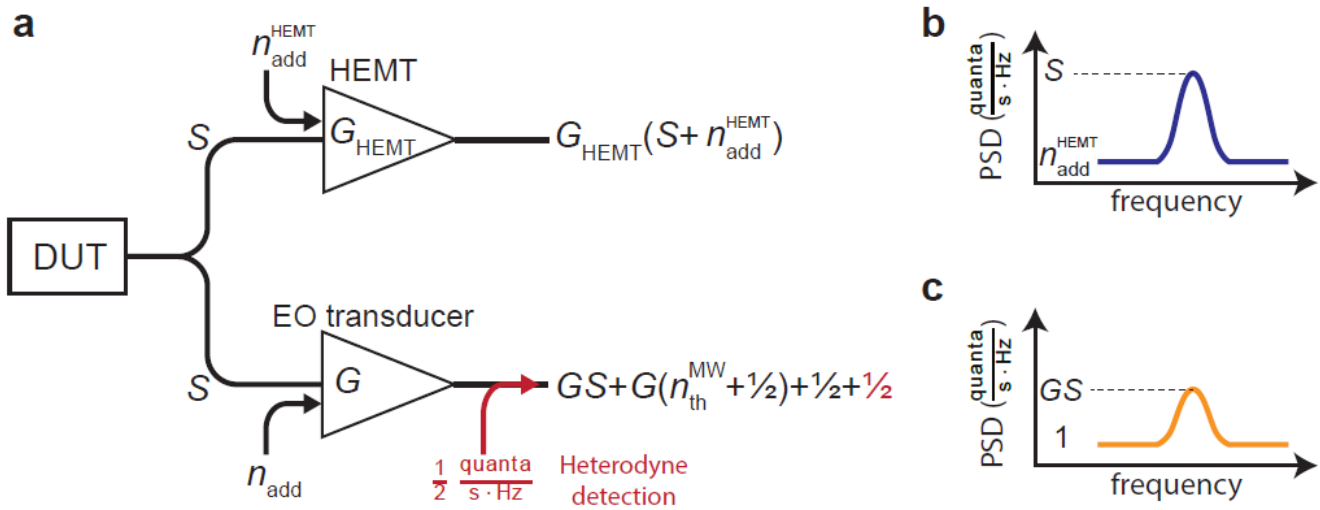


Figure 5

Illustration of the gain characterization procedure. a, Propagation of the DUT signal through the system. b, Power spectral density of the HEMT output. c, Power spectral density of the optical heterodyne detector.

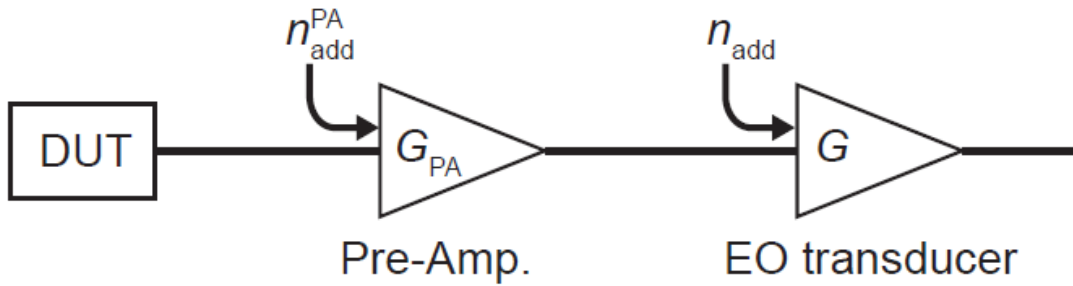


Figure 6

Schematic signal flow when pre-amplifier is used.

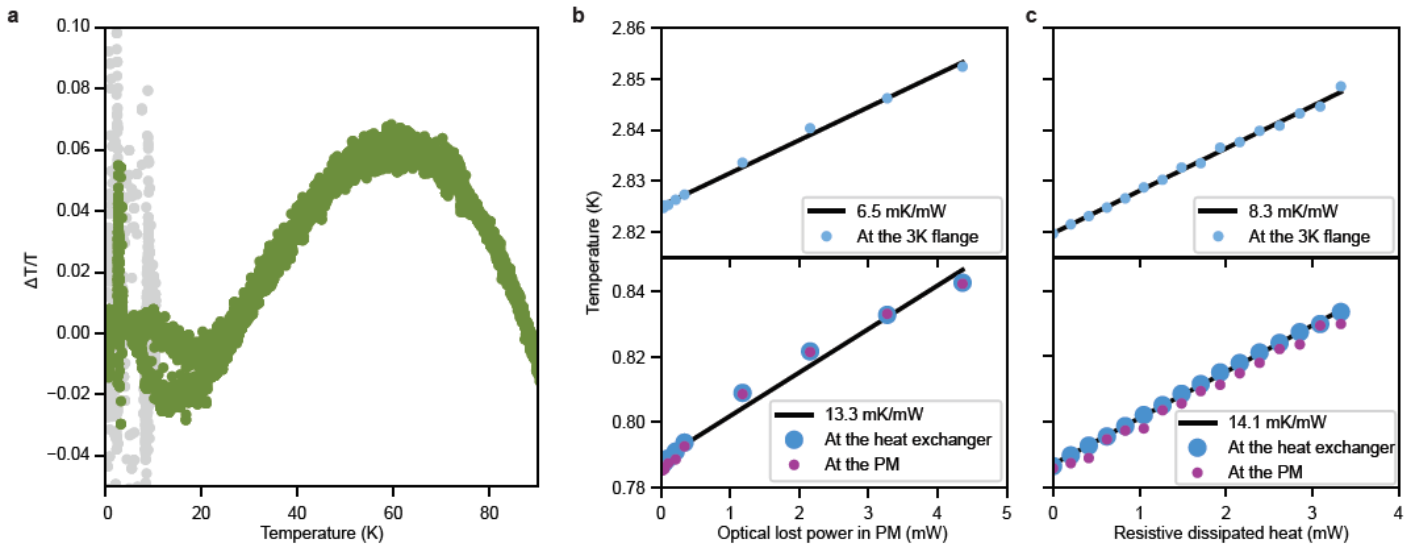


Figure 7

Heat dissipation and temperature gradients. a, Relative temperature difference between PM box and heat exchanger, on 800mK flange during a cooldown. The gray datapoints correspond to specific periods of pulse precooling and mixture condensation, where the temperature is unstable. b, Measurement of heating due to optical dissipation when the phase modulator is mounted on the 800mK flange. c, Measurement of heating using a calibrated resistive heater mounted on the 800mK flange.